

Formation of the oxyl's potential energy surface by the spectral kinetics of a vibrational mode

James Stewart¹, Paul Zayka¹, Christen Courter¹ and Tanja Cuk^{*,1,2,3}

¹Department of Chemistry, University of Colorado, Boulder, Colorado 80303, United States

²Renewable and Sustainable Energy Institute (RASEI), University of Colorado, Boulder, Colorado 80303, United States

³Materials Science and Engineering Program (MSE), University of Colorado, Boulder, Colorado 80303, United States

KEYWORDS (catalytic mechanism, oxyl radical, oxygen evolution reaction, ultrafast vibrational spectroscopy, polaron formation).

[‡]These authors contributed equally to the work

ABSTRACT: One of the most reactive intermediates for oxidative reactions is the oxyl radical, an electron-deficient oxygen atom. The discovery of a new vibration upon photoexcitation of the oxygen evolution catalysis detected the oxyl radical at the SrTiO₃ surface. The vibration was assigned to a motion of the sub-surface oxygen underneath the titanium oxyl (Ti-O[•]), created upon hole transfer to (or electron extraction from) a hydroxylated surface site. Evidence for such an interfacial mode derived from its spectral shape which exhibited a Fano resonance—a coupling of a sharp normal mode to continuum excitations. Here, this Fano resonance is utilized to derive precise formation kinetics of the oxyl radical and its associated potential energy surface (PES). From the Fano lineshape, the formation kinetics are obtained from the anti-resonance (the kinetics of the coupling factor), the resonance (the kinetics of the coupled continuum excitations), and the frequency integrated spectrum (the kinetics of the normal mode's cross-section). All three perspectives yield a logistic function growth with a half-rise of 2.3 ± 0.3 ps and rate of 0.48 ± 0.09 ps. A non-equilibrium transient associated with photoexcitation is separated from the rise of the equilibrated PES. The logistic function characterizes the oxyl coverage at the very initial stages ($t \sim 0$) to have an exponential growth rate that quickly decreases towards zero as a limiting coverage is reached. Such time-dependent reaction kinetics identify a dynamic activation barrier associated with the formation of a PES and quantify it for an oxyl radical coverage.

1

2 INTRODUCTION

3 Surface oxygen intermediates form the basis of reaction mechanisms of heterogeneous catalysis on metal
4 oxides. Their coverages and formation rates guide the evolution of reactants into products. One of the
5 most reactive surface oxygen species is considered the oxyl radical with an electronic configuration of
6 O[•]. For example, the oxyl radical has been invoked to explain O-O bond formation within the oxygen
7 evolution reaction (OER) from water¹⁻². In bi-radical recombination, two oxyls reduce their electron de-
8 ficiency by forming a bond between the two radicals³⁻⁴.

9 On a surface, the oxyl radical is bound to a metal site, forming a terminal M-O[•]. When produced elec-
10 trochemically during OER, electrons and protons are taken from a water adsorbed species within the
11 hydration layer of the metal-oxide⁵⁻⁶. The microscopic details of how the electron and proton transfers⁷⁻⁸
12 arise determine the oxyl's binding energy and kinetic stability with respect to the initial catalyst surface⁹
13 and therefore, its ability to catalyze the rest of the cycle. To arrive at these microscopic details, it would
14 be important to follow how the excited state potential energy surface (PES) of a stable population of oxyls
15 forms.

16 When photons drive the electrochemistry by photo-electrochemistry at a semiconductor-liquid interface,
17 the necessary time resolution exists to track radical formation. In recent years, diverse optical probes of
18 photo-electrochemically excited OER from an electron doped SrTiO₃/electrolyte interface have investi-
19 gated the formation of surface oxygen intermediates¹⁰⁻¹⁵. A critical one is the mid-infrared probe of the
20 vibrational structure of the surface bound oxyl radical¹². A molecular vibration near the longitudinal
21 optical phonon of SrTiO₃ was observed to form upon valence band hole transfer to (or electron transfer
22 from) a hydroxylated site. The hole transfer occurs alongside proton transfer from the hydroxylated group
23 to a neighboring, bare oxygen site. The assignment was made using experimental correlations, density
24 functional theory calculations of the excited state PES, and connections between them. The detailed
25 theoretical calculation was required, because unlike an oxo such as Co=O,⁹ a new bond is not created
26 when the intermediate is formed. One of the experiment-theory connections is the spectral shape of the
27 mode, which exhibits a Fano resonance¹⁶. In a Fano resonance, a narrow vibrational mode couples to a
28 broad continuum (*e.g.* excitations of delocalized carriers) that are also excited by the infrared probe. They
29 can be quite informative on how molecular structures couple to an extended, solid-state environment. For
30 example, Fano resonances describe plasmonic interactions between quantum nanocrystals and colloidal
31 molecules¹⁷ and adsorbed molecular catalysts¹⁸.

32 Here, we use the oxyl radical's vibration and the associated Fano resonance to determine the reaction
33 kinetics by which the hole traps and the oxyl radical forms. The reaction kinetics are obtained through
34 three characteristics and associated parameters of the Fano lineshape: the anti-resonance (the kinetics of
35 the coupling factor), the resonance (the kinetics of the coupled continuum excitations), and the frequency
36 integrated spectrum (the kinetics of the normal mode's cross-section). That all three perspectives yield a
37 logistic function growth with a half-rise of 2.3 ± 0.3 ps and rate of 0.48 ± 0.09 ps suggests that we are
38 tracking the formation of the excited state PES through its underlying quantum states. To show the meth-
39 odology, a particular electron doping (0.7% Nb) and an air interface is chosen; the air interface contains
40 a hydration layer but no solvent. The logistic function describes an exponential growth rate at the very
41 initial stages ($t \sim 0$) that quickly decreases towards zero as a limiting oxyl coverage is reached. A transient,
42 non-equilibrium signal exists that is separated out in the analysis. While such non-equilibrium effects are
43 anticipated and intrinsically interesting, we focus on the logistic growth that resolves a dynamic activation
44 barrier in the formation of an excited state PES.

45

46 SPECTRAL KINETICS OF OXYL RADICAL FORMATION

47 An ultraviolet light pulse first excites the wide-band gap semiconductor SrTiO₃ (STO) to create delocal-
48 ized electrons and holes in the conduction and valence band respectively. In Figure 1a, this is depicted
49 by the pump pulse that takes the ground state of the perovskite (1) to the excited state (2) containing
50 delocalized holes on the largely O 2p valence band. The holes can preferentially trap at a distorted reaction
51 coordinate in early transition metal oxides¹⁹⁻²¹. If they form on hydrated sites, they can form reactive
52 surface oxygen species (3) trapped by the polarization of the distortion²²⁻²³. At the new reaction coordi-
53 nate, the vibrational transitions (3→4) are characteristic of the surface oxygen species created.

54

55 That such a process is relevant to Nb-doped SrTiO₃ (n-STO) and creates meta-stable oxyl radicals was
56 investigated previously. Figure 1b summarizes the results by showing the density functional theory cal-
57 culation of the vibrational structure of the surface of the metal-oxide for the ground state PES, with the
58 hydration layer alone (left) and for the excited state PES (right), containing a coverage of terminal titanium
59 oxyl radicals (Ti-O•)¹². In place of the symmetric breathing mode in the ground state, an optically active
60 one appears due to the sub-surface oxygen motion perpendicular to the surface and directly underneath
61 the oxyl radical. The experimental conditions introduced methanol scavengers and correlated the observed

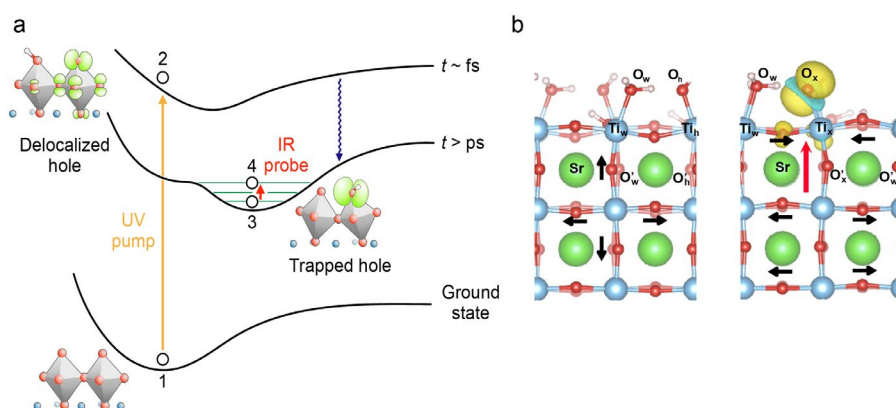
62 vibration with O₂ evolution to show that the mode occurred when holes could efficiently trap to the sur-
 63 face¹². The experimental conditions also varied the doping of the semiconductor¹². For electron doped
 64 STO by Nb, the electric field at the interface drives holes to the surface and the mode is observed, while
 65 hole doped STO by Fe, the electric field is in the opposite direction and the mode is not observed. As
 66 probed by its vibrational mode, the oxyl radicals were found to be stable through nanoseconds.

67

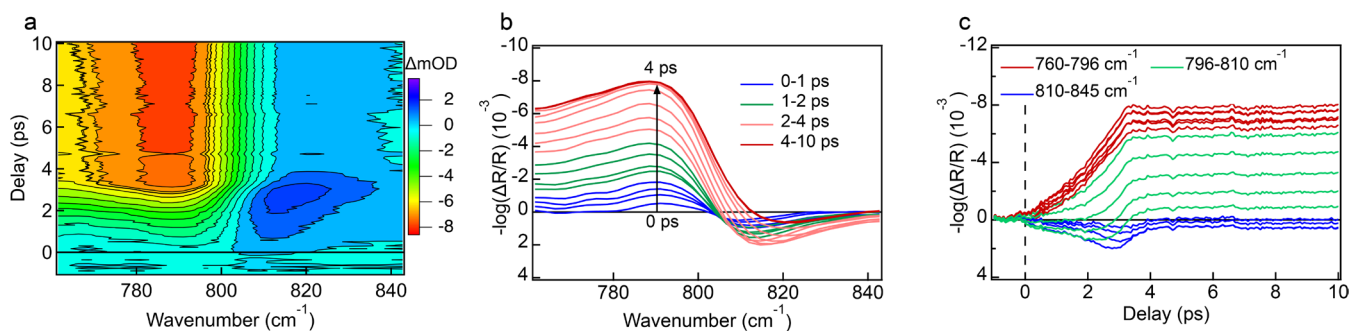
68 As introduced above, the vibrational mode exhibits a characteristic Fano resonance in which the mode
 69 couples to neighboring continua. In the case of the oxyl radical's vibration, the resonance exists both with
 70 the continuum of the solid (a plasma excitation, delocalized carrier excitations) and of the liquid (a libra-
 71 tional excitation of water). Previous work makes this conclusion by modulating the extent of the contin-
 72 uum involved through doping the solid, comparing air to liquid interfaces, and deuterating the water¹².
 73 That the vibration couples to continua within the solid and the liquid shows that it truly sits at the interface,
 74 connecting the experimental phenomenology to the density functional theory calculations. In the follow-
 75 ing work, we have chosen the air interface and the highest doping, 0.7 wt. % Nb, for which the continuum
 76 of the solid dominates. When coupled to the vibrational mode, the plasma oscillations of the doped elec-
 77 trons are polarized to screen the vibrational dipole; the signal of both the mode and the continuum are
 78 seen only in p-polarization when the incoming light beam has a component perpendicular to the sample
 79 plane¹².

80

81 In-situ ultrafast IR spectroscopy in an attenuated total reflectance (ATR) geometry measures the subsur-
 82 face vibrational mode. In this technique, an evanescent wave formed by total internal reflectance between
 83 the ATR crystal, a single bounce diamond, and air probes the sample surface²⁴. As opposed to a propagat-
 84 ing wave, the evanescent wave cannot couple directly to optical phonons of a bulk crystal due to a spatially
 85 decaying Poynting vector, such that the signal is dominated by surface modes. The STO crystal is brought
 86 close enough to the diamond to be within the ~ 1 μm evanescent decay of the mid-infrared probe²⁵.
 87 The data is reported at each time delay as a change in the probe reflectance (ΔR) before and after above band
 88 gap pump (266 nm) excitation, calculated using optical density or $\Delta \text{mOD} = -\log(\Delta R/R) \cdot 10^{-3}$. The beam
 89 is p-polarized with a 60° angle to the sample normal. A more detailed description of the experimental
 90 configuration can be found in Supplemental Figure 1.



91 **Figure 1.** Potential energy surface (PES) and vibrational probe of the oxyl radical. a) PES of the ground
 92 state of SrTiO₃ at its minimum (1), the excited state PES of delocalized holes upon UV photoexcitation
 93 (2), and after the PES equilibrates, such that the hole traps in a new minimum of the reaction coordinate
 94 (3) that can be probed by a mid-infrared vibration (4). b) On the right, the oxyl radical's (yellow, spin
 95 orbital) subsurface vibration (red arrow) formed from a linear combination of dark (black, breathing)
 96 modes prior to excitation of the hydrated surface on the left.



98

99 **Figure 2.** Time evolution of the vibrational signal of the n-STO air interface in the first ten ps following
 100 excitation. The 2D contour plot (a) and associated spectra (b) and kinetic traces (c) depict the picosecond
 101 rise of the oxyl radical's vibration. The vibrational peak begins to take shape within the first picosecond
 102 and reaches its final, converged lineshape by 4 ps. The y-axis of (b) and (c) correspond to the Δ mOD
 103 color scale of the contour plot (a) and represent a change in absorption based on Beer's Law, or Δ mOD
 104 = $-\log(\Delta R/R) \cdot 10^{-3}$ where R is the reflectance.

105 The initial ten picoseconds of the oxyl radical's formation is illustrated in Figure 2. In the contour plot
 106 (Figure 2a), substantial changes occur within the first four picoseconds until the signal converges to a
 107 final, unchanging spectral shape. The contour plot exhibits a distinctively asymmetric spectral shape, with
 108 a peak optical density (red) at 786 cm⁻¹. On the higher frequency side of the peak, the optical density
 109 drops sharply while on the lower frequency side, it drops gradually. This asymmetry aligns with expect-
 110 ations for a Fano resonance, as will be explored in more detail below. The optical density of the Fano
 111 peak is negative due to the refractive indices involved in the attenuated total reflection geometry, as dis-
 112 cussed elsewhere. A transient background also exists—the short-lived positive optical density (dark blue)
 113 on the higher frequency side of the peak.

114 Spectral slices at specific delays are shown in Figure 2b. While the signal grows in, the spectral width
 115 also increases as seen by the peak to valley distance in the blue (0-1 ps) versus pink (2-4 ps) spectra. The
 116 transient background, with a positive maximum near 810 cm⁻¹, grows in and then decays. Kinetic traces
 117 at specific frequencies are shown in Figure 2c. There are three regimes: green for frequencies near the
 118 Fano resonance (796-810 cm⁻¹, as will be determined below), red for frequencies below this Fano reso-
 119 nance (760-796 cm⁻¹), and blue for frequencies higher than this Fano resonance (810-845 cm⁻¹). For the
 120 wavenumbers covered within the blue frequency regime, the transient background dominates while for
 121 those covered by the red frequency regime, the signal of the Fano peak dominates. For both the spectral
 122 slices and the kinetic traces, the data demonstrate a converged signal by 4 ps.

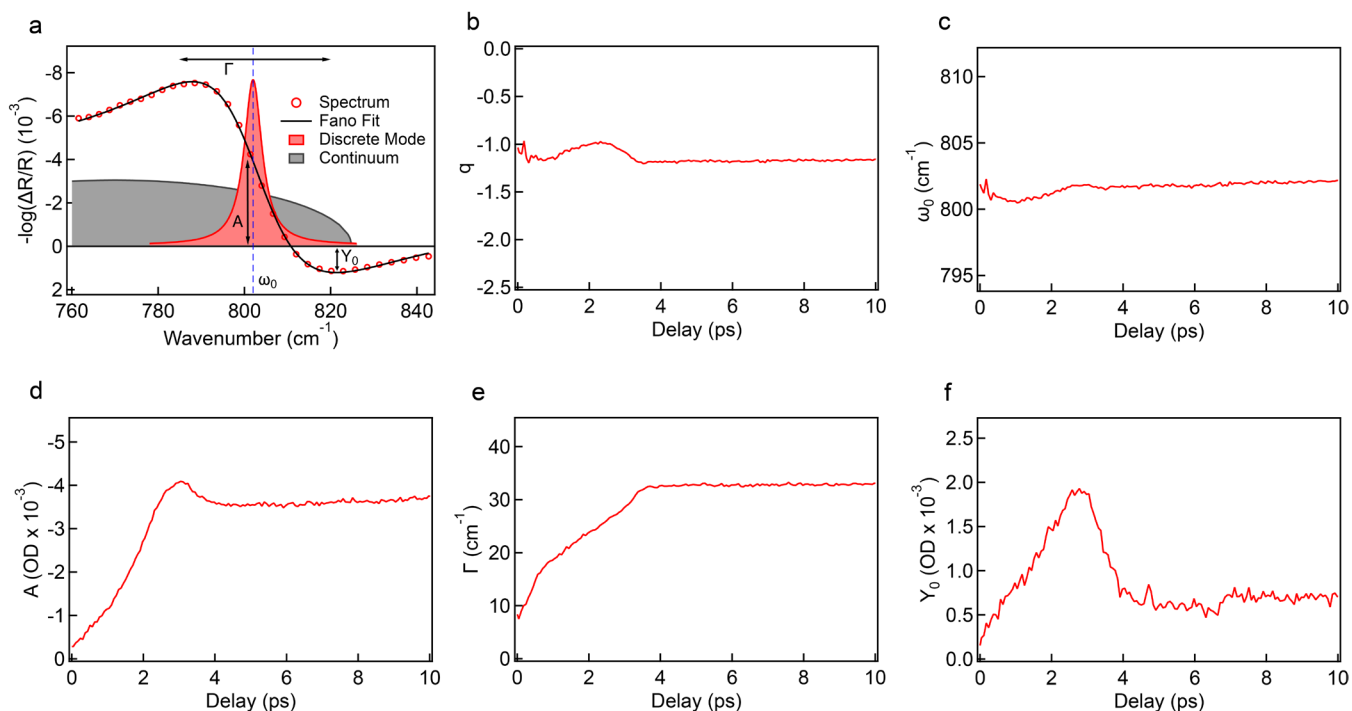
123 The presented data underwent two separate procedures to eliminate artifacts and background signals. First,
 124 regular oscillations in wavenumber are observed, likely due to the mid-infrared detection electronics.
 125 Since these oscillations have a constant frequency spectrum in time and are additive to the oxyl signal,
 126 they can be removed using a low pass FFT filter, as shown in Figure S2a. Second, a background due to
 127 the pump-probe response from the diamond ATR crystal is taken without the presence of the STO sample
 128 after each measurement and subtracted out. While the bandgap of diamond is above that of the pump
 129 beam (5.5 eV vs 4.7 eV), pump-probe responses in the IR range at similar pump wavelengths (273 nm,
 130 310 nm) and peak fluences (\sim GW/cm²) have been attributed to two photon absorption²⁶⁻²⁷. Since the
 131 diamond response is also generally a narrow, symmetric peak about time zero, it has been used as an
 132 autocorrelation measurement of the pump and probe²⁷. We have a similarly symmetric peak (Figure S2b)
 133 and use it to determine time zero by a gaussian fit (Figure S2c).

134 The instrument response function (IRF) was measured previously by a cross-correlation of the pump pulse
 135 (266 nm) with a 150 fs, 800 nm pulse, determining a pulse width of 0.4 ps (Figure S3a). This resolution
 136 is sufficient to accurately resolve the rise without distorting the kinetics. A convolution of the IRF with
 137 the logistic function used for fitting the reaction kinetics (discussed below) yielded a fit that is unchanged
 138 in comparison to the non-convolved logistic function (Figure S3b).

139 In parallel to the data presented in Figure 2 and analyzed within the manuscript, two other data sets taken
 140 with the same experimental conditions were measured and analyzed. The contour plots, spectral slices,
 141 and kinetic traces of all three data sets are shown in Figure S4, highlighting the reproducibility of the
 142 measurements. While the overall signal strength varied due to the ATR geometry's sensitivity to the
 143 distance between the ATR crystal and the sample, the time-dependent spectra are consistent across the
 144 three data sets.
 145

$$|\langle Y|T|i\rangle|^2 = \frac{A(t) \left(\frac{2(\omega - \omega_0)}{\Gamma(t)} + q \right)^2}{1 + \left(\frac{2(\omega - \omega_0)}{\Gamma(t)} \right)^2} + Y_0 \quad \text{Equation. 1}$$

146



147

148 **Figure 3.** Free-form Fano fits of the spectral kinetics. (a) Illustrates the Fano fit (black line) that results
 149 from excitation of the discrete mode (gray) and the coupled continuum (gray) by the infrared probe to
 150 detect the resulting asymmetric spectrum (red dots). (b)-(f) show the time evolution of the Fano param-
 151 eters obtained from free fits: (b) The Fano asymmetry constant (q), (c) the resonant frequency (ω_0), (d) the
 152 coupled continuum excitations (A), (d) the coupling factor (Γ), and the uncoupled continuum excitations
 153 (Y_0).

154 Next, we turn to examining the data using the Fano lineshape, whose form is given by Equation 1. There
155 are several quantum mechanical wave functions involved in the Fano equation¹⁶. Ψ represents the vibra-
156 tional wave function coupled to the continuum, such that $|\langle\Psi|T|i\rangle|^2$ is the square of the transition dipole
157 moment or intensity measured by the spectroscopy for the coupled vibrational mode; T is the dipole op-
158 erator and i is the initial state. ψ is the quantum mechanical wave function of the continuum and A in eq.
159 1 denotes $|\langle\psi|T|i\rangle|^2$, or the intensity of the continuum light excitations coupled to the mode. Y_0 is the
160 same, but for the uncoupled continuum excitations; it is an additive, constant background in the region of
161 the mode frequency. The lineshape is a function of $(\omega - \omega_0)/2\Gamma$. ω_0 is the resonant frequency of the mode
162 after coupling to the continuum. Γ is equal to the square of the coupling constant of the mode to the
163 continuum and is a measure of the spectral width; with $q=0$, the Fano equation simplifies to a Lorentzian.
164 For a given Γ , the light frequency ω probes the Fano lineshape through the resonance.

165 Figure 3a shows representations of the bare vibrational mode, the continuum excitations, and the Fano
166 lineshape of the coupled vibrational mode. Fano parameters A (an intensity at $\omega=\omega_0$), Γ (a spectral width),
167 ω_0 (the resonant frequency), and Y_0 (constant background) on the Fano lineshape are depicted. The main
168 continua contributing to the Fano lineshape come from electron plasma and delocalized carrier excitations
169 in the STO substrate²⁸. The electronic plasma continuum is a broad peak centered at 400-500 cm^{-1} and
170 extends past the 802 cm^{-1} vibrational mode, as represented by the gray spectrum. In addition to this, there
171 are delocalized carrier excitations due to both dopant electrons and electron-hole pairs created upon pump
172 excitation.

173 The coupling between the mode and the continuum results in an asymmetric lineshape when light simul-
174 taneously excites the mode and the coupled continuum. That asymmetry is defined by the parameter q :

175
$$q^2 = \frac{2|\langle\phi|T|i\rangle|^2}{\pi|\langle\psi|T|i\rangle|^2\Gamma} \quad \text{Equation 2}$$

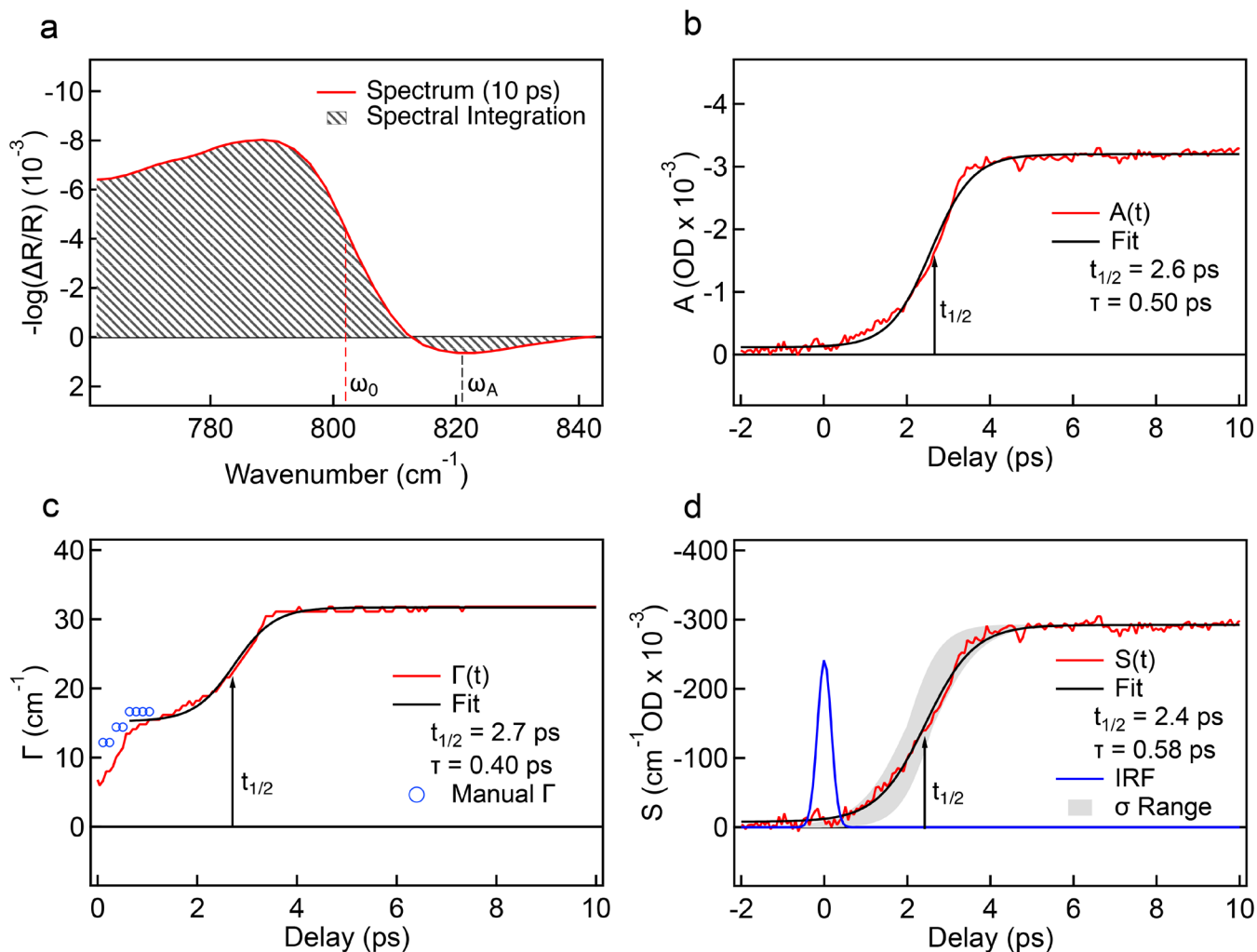
176 Thus, q^2 is proportional to the ratio of light excitations of the bare but dielectrically screened mode
177 ($|\langle\phi|T|i\rangle|^2$) to that of the coupled continuum light excitations ($|\langle\psi|T|i\rangle|^2$). The denominator represents the
178 number of continuum excitations that contribute to the Fano resonance within the width of the mode,
179 given by Γ ; ψ is reported as a density of states such that q is unitless. For our data, with a q value near -
180 1, Γ is the difference between the maximum and minimum of the Fano peak, as depicted in Figure 3a.

181 The spectra shown in Figure 2b were freely fit with the Fano lineshape at each time delay. The quality of
182 the fits for the main manuscript data are shown in Figure S5. The resulting time-dependence of the Fano
183 parameters are shown in Fig. 3b-3f. Interestingly, the asymmetry parameter q (Fig. 3b) and the resonant
184 frequency ω_0 (Fig. 3c) are fairly time independent. The coupled continuum excitations of A (Fig. 3d) and
185 the coupling factor defined by Γ (Fig. 3e) both exhibit rising kinetics that converge to a final value by 4
186 ps, while the uncoupled continuum excitations of Y_0 (Fig. 3f) rise and decay by 4 ps. In addition, a
187 transient can be seen in A before the kinetics stabilize.

188 Free fits performed on all three data sets are shown in supplemental figure S6. While overall similar trends
189 for each parameter are shown, some parameters are highly correlated and changing one can be compen-
190 sated by changing another. An example of when this occurs is the third data set for which q becomes time
191 dependent, and A has a different time dependence than that shown in Fig. 3d. Thus, one set of free fits is
192 not necessarily unique.

193

194



195

196 **Figure 4.** Extraction of $A(t)$, $\Gamma(t)$, and $S(t)$ by frequency regimes of the Fano resonance. (a) Depicts the
 197 resonant frequency (ω_0) and anti-resonant frequency (ω_A) used to determine $A(t)$ and $\Gamma(t)$ respectively on
 198 the 10 ps spectrum. The frequency integrated spectrum is $S(t)$. (b-d) show the time evolution of $A(t)$ (b),
 199 $\Gamma(t)$ (c), and $S(t)$ (d) along with the corresponding logistic fits and associated time constants. The manual
 200 determination of $\Gamma(t) < 1$ ps is shown in (c). The instrument response function (IRF) and standard deviation
 201 range of the data (σ range) are given in (d).

202 EXTRACTING TIME-DEPENDENCE OF FANO PARAMETERS: $A(t)$, $\Gamma(t)$, and $S(t)$

203 Fortunately, distinct frequencies within the Fano lineshape uniquely determine $A(t)$ and $\Gamma(t)$ if q and ω_0
 204 are constant. The constancy of q and ω_0 is on the one hand supported by the free fits, for which it generally
 205 occurs. On the other hand, conceptually the constancy of q can be understood by its construction from
 206 the underlying quantum mechanical wave functions of the two parts contributing to the Fano resonance:
 207 a ratio of the light excitations of the bare mode (the numerator) to those of the coupled continuum within
 208 the mode's width (the denominator). If as the bare mode forms, it couples at each instant to the continuum,
 209 then q should be constant in time. Similarly, if the coupling occurs at each instant, the resonant frequency
 210 should be constant in time. A justification for such an instantaneous coupling is that the electronic re-
 211 sponse to atomic motion is considered fast on the time scale of the atomic motion itself. The Born-
 212 Oppenheimer approximation is an example of such a justification, albeit for how electrons in a bond

213 respond to atomic motion. We will return to this justification below with data itself and a frequency
214 integration of the Fano lineshape.

215 If q and ω_0 are time-independent, then the Fano lineshape evaluated at the resonant frequency uniquely
216 extracts the time evolution of the coupled continuum excitations ($A(t)$). At the resonant frequency, Equa-
217 tion 1 simplifies to:

$$218 \quad |\langle \Psi | T | i \rangle|^2 = A(t) \cdot q^2 \quad \text{Equation 3}$$

219

220 From the free fits, ω_0 and q were determined to be 802 cm^{-1} (Figure 3c) and -1.2 (Figure 3b) respectively.
221 For a q near -1 , ω_0 is located at approximately the half-rise of the peak (Figure 4a). Using these values,
222 $A(t)$ shown in Figure 4b exhibits an S-shaped growth that saturates beyond 4 ps and does not contain the
223 transient of the free fits (Figure 3d).

224 Similarly, the anti-resonance frequency (ω_A) can be used to determine the time evolution of the coupling
225 factor ($\Gamma(t)$). The anti-resonance is located at the minimum of the concavity in the Fano lineshape, as
226 labeled in Figure 4a. In the absence of a constant offset (Y_0), ω_A occurs at the zero of the Fano lineshape,
227 such that:

$$228 \quad \omega_A = \frac{-q\Gamma(t)}{2} + \omega_0 \quad \text{Equation 4}$$

229 Given the existence of an offset, extracting ω_A from the data is done by taking the first and second deriv-
230 atives of the spectrum to find the frequency at which the first derivative is zero and the second derivative
231 is negative (Figure S7a). Once this frequency is extracted at each time delay, $\Gamma(t)$ is derived from Equation
232 4 with $\omega_0 = 802 \text{ cm}^{-1}$ and $q = -1.2$. The resulting time evolution is shown in Figure 4c and like $A(t)$,
233 exhibits an S-shaped growth that saturates by 4 ps.

234 At the earliest time delays, the data do not fit perfectly to a Fano lineshape which especially affects the
235 extraction of $\Gamma(t)$. The method to extract ω_A uses the Fano fits of each spectrum rather than the data itself
236 because the point density in the fit is much greater than the data (taken at each pixel of the detector) and
237 produces a smooth $\Gamma(t)$ in comparison (Figure S7b). This results in a value of Γ that does not accurately
238 reflect the anti-resonance at the earliest time delays (Figure S7c). Therefore, for these time delays, ω_A are
239 extracted manually and the resulting Γ values are shown as blue circles in Figure 4c. Nonetheless, a
240 change in $\Gamma(t)$ is noticeable below 0.75 ps. Even faster processes could be at play in the hole trapping
241 reaction, and we do not attempt to ascribe their origin here.

242 We now turn to one more way of extracting the time dependence of the Fano parameters and that is
243 through a frequency integration of the spectrum at each time delay. The resulting $S(t)$ is shown in Figure
244 4d. Interestingly, like $A(t)$ and $\Gamma(t)$, $S(t)$ exhibits an S-shaped growth that saturates. As derived by U
245 Fano¹⁶, the integration, S , of the Fano lineshape represents the cross-section of the bare, screened mode
246 after a simple subtraction of the coupled continuum excitations (A), integrated over the same frequency
247 range. Without this correspondence, the frequency dependence of the underlying parameters invalidates
248 the derivation of the Fano resonance. That $S(t)$ exhibits a regular growth and one that resembles $A(t)$
249 supports the applicability of the Fano resonance here. Furthermore, it suggests that the cross-section of
250 the bare, screened mode is created essentially at the same time as that of the cross-section of the coupled
251 continuum excitations, which helps justify the constancy of q and ω_0 described above.

252 The S-shaped growth of A(t), $\Gamma(t)$, and S(t) suggests the use of a logistic growth function (Equation 5) to
253 describe the kinetics. This yields two-time constants, along with the saturation of the growth (max): τ ,
254 which describes the rate of the rise, and $t_{1/2}$, which defines the half-rise of the growth²⁹. The logistic
255 function used to fit the data is:

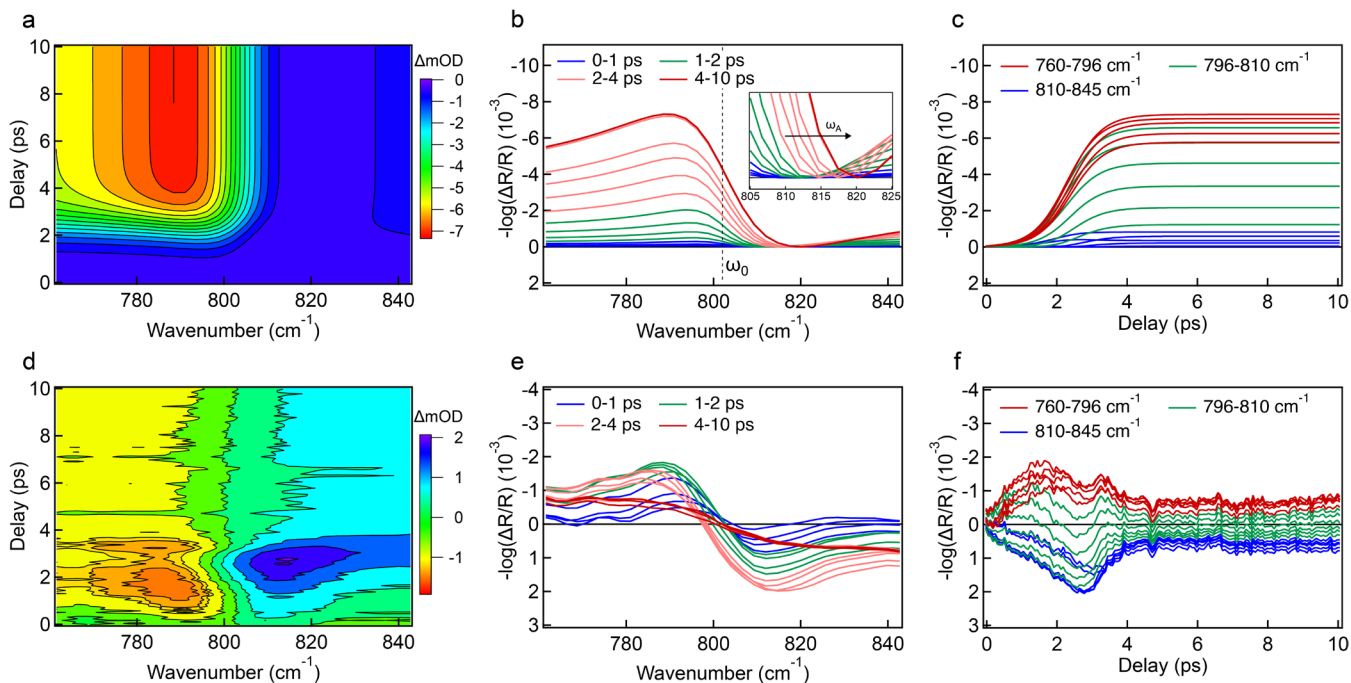
256
$$f(t) = \frac{\text{max}}{\left(1 + \exp\left\{\frac{t_1 - t}{\tau}\right\}\right)} + \text{base} \quad \text{Equation 5}$$

257 Base is a constant background used especially for fitting $\Gamma(t)$ starting at 0.75 ps. The fits, shown on top
258 of the data in Figure 4, nicely describe the growth kinetics of all three Fano parameters.

259 Furthermore, they all exhibit similar τ and $t_{1/2}$ values. Each of the three data sets yields three evaluations
260 of these time constants by A(t), $\Gamma(t)$, and S(t). The results are shown in Figure S8 and the time constants
261 are compiled in Table S1. The nine separate determinations of the time constants lead to the following
262 average values and standard deviations: $\tau = 0.48 \pm 0.09$ ps and $t_{1/2} = 2.3 \pm 0.3$ ps. The range of logistic
263 curves given by the average values \pm one standard deviation is displayed in Figure 4d in gray and detailed
264 in Figure S9, which also describes the effect of changing τ and $t_{1/2}$ individually. The IRF on Figure 4d
265 shows that the time-resolution would not affect the fits.

266 An exponential rise of the form $1 - e^{-t/\tau}$ (Equation S2) is often used to fit the reaction kinetics of similar
267 systems following light excitation. To explore the validity of such a fit, A(t) extracted at the resonant
268 frequency (801 cm^{-1}) (Figure S10a) and the kinetic trace at the Fano peak maximum (786 cm^{-1}) (Figure
269 S10b) were each fit by an exponential rise. A time-zero offset between 0 ps and 2 ps was included to
270 account for any time dynamics that were not measured by the probe (*e.g.* of delocalized carriers). For the
271 exponential rise to capture the second half of A(t), the fit must be initialized with an offset of 2 ps, which
272 results in a failure to capture the initial time delays at all. The same occurs for the kinetic trace at the peak
273 maximum, which rises faster than A(t) and yet, the simple exponential cannot fully capture both ends of
274 the time trace. Thus, the logistic function represents a more accurate and holistic function with which to
275 model the oxyl formation kinetics by its specific vibration. The logistic formation is different than the
276 rising exponential fits of the visible stimulated emission or the coherent terahertz oscillations that provide
277 information on the electronic levels¹¹ and the continuum lattice strain¹⁵ due to hole-polarons on n-STO
278 respectively. When probed in a more collective way, for which different geometries of hole-traps are not
279 distinguished, a rising exponential can be fit with a 1.3 ps time-constant. We also note that the kinetics
280 at the Fano peak maximum (Figure S10b) and away from resonance are different than that extracted by
281 the Fano parameters.

282



283

284 **Figure 5.** Modelling the equilibrated PES of the oxyl and the non-equilibrium transient. (a) Contour plot of the Fano resonance of the equilibrated PES with associated spectral slices (b) and kinetic traces (c).
 285 of the Fano resonance of the equilibrated PES with associated spectral slices (b) and kinetic traces (c).
 286 The input parameters for q , ω_0 , $\Gamma(t)$, and $A(t)$ are described in the text. (d)-(f) show the difference between the raw data (Figure 2) and the model for the equilibrated PES (a-c), which extracts the contour plot (d),
 287 spectral slices (e), and kinetic traces (f) of the non-equilibrium transient.
 288

289 REACHING AN EQUILIBRIUM POTENTIAL ENERGY SURFACE OF OXYL RADICALS

290 By using the kinetics extracted by the resonant frequency for $A(t)$, of the shift in the anti-resonant frequency for $\Gamma(t)$, and the frequency integrated spectrum for $S(t)$, a common logistic function rise was found
 291 with a τ of 0.48 ps and a $t_{1/2}$ of 2.3 ps. Since the logistic function exhibits a smooth increase that then
 292 saturates, it cannot itself describe transients within the data. In the following, we utilize this finding to
 293 separate components of the data that describe an equilibrium reached by a meta-stable excited state surface
 294 from a decaying transient. We then consider what the kinetics of this equilibration say about the mechanism
 295 of hole-trapping to create the excited state PES of oxyl radicals.
 296

297 To separate out the formation of the excited state PES, a Fano lineshape is built from the two time-independent
 298 parameters, q and ω_0 , and the two time-dependent parameters, $A(t)$ and $\Gamma(t)$. Figure 5a shows
 299 the contour plot of a Fano equation with $q=-1.2$ (Figure 3b), $\omega_0=802 \text{ cm}^{-1}$ (Figure 3c), and logistic function
 300 growths for $A(t)$ and $\Gamma(t)$ with $\tau = 0.48$ and $t_{1/2} = 2.3$. For $A(t)$, the logistic function rises from zero (base)
 301 to a maximum of 3 mOD (max) as derived from Figure 4b. For $\Gamma(t)$, a base of 15 cm^{-1} rises by 15 cm^{-1}
 302 (max) to saturate at 30 cm^{-1} as derived from Figure 4c.

303 Select spectral slices at 1-2 ps, 2-4 ps, and 4-10 ps are shown in Figure 5b. As depicted there, ω_0 is
 304 constant, while ω_A redshifts. The redshift is anticipated from Eq. 4 as Γ grows in time. While such a
 305 redshift can be seen in the data itself (Figure 2b), it becomes clearer in the modelling for which the transient
 306 Y_0 is not included. Select kinetic traces prior to ω_0 , near ω_0 , and through ω_A are shown in Figure
 307 5c. Both the kinetic traces and the spectral slices for $\omega > \omega_A$ more clearly show the tail of the Fano
 308 lineshape obscured in the data by the transient Y_0 (Figure 2c). Overall, the spectral and kinetic traces follow
 309 that of the raw data (Figure 2b-c) when the uncoupled background is avoided either in frequency (< 800
 310 cm^{-1}) or in time (> 4 ps).

311 To identify the transient in the data, we have subtracted this equilibrium model from the raw data to obtain
312 the contour plot in Figure 5d. The spectral slices and kinetic traces are shown for select time delays and
313 frequencies in Figure 5e and Figure 5f. The entirety of the signal is transient and there are two compo-
314 nents: a peak in the region of the anti-resonance, and a fairly symmetry peak of opposite sign below the
315 resonance. Interestingly, at the resonant frequency, there is a negligible transient. The two components
316 reflect the transient $Y_0(t)$ and the transient within $A(t)$ seen in the free Fano fits of Figure 3f and 3d
317 respectively. While the background to the Fano lineshape is then frequency dependent, it is also of a
318 particular shape such that the kinetics extracted at ω_0 , by the shift in ω_A , and the integrated spectrum
319 isolate the kinetics of equilibration. The non-equilibrium component is avoided at the resonant frequency,
320 does not appreciably change the anti-resonant frequency, and being approximately symmetric across the
321 resonance, integrates to \sim zero within the frequency window. While this is the outcome of the data anal-
322 ysis using the distinctive Fano lineshape, why such a clean separation is possible is not a priori clear and
323 would require an atomistic understanding of how non-equilibrium transients couple to the vibration as the
324 PES forms. One of the possible origins of the non-equilibrium transient are electron-hole excitations by
325 the pump that couple to the vibration temporarily before they decay.

326 We now turn to how to visualize populating an electron doped semiconductor surface with oxyl radicals
327 using a logistic function rise and further, one that is consistent across several Fano parameters. Each of
328 the parameters have a distinct physical meaning, as discussed in detail above. $S(t)$ is a measure of the
329 transition dipole of the bare, screened vibration while $A(t)$ and $\Gamma(t)$ are measures of how that vibration
330 couples to its surroundings. Since they all rise with a similar logistic function suggests that as the oxyl
331 forms, the vibration simultaneously couples to the electronic continuum. One could rationalize this result
332 by the time required for a change in the vibrational dipole moment to couple to the electronic continuum,
333 which could be instantaneous at the time-resolution of the experiment as discussed above.

334 On the other hand, the logistic function growth is itself more difficult to describe, since it means that the
335 reaction kinetics change in time as the oxyl forms. In the $t=0$ limit, the rate of growth is exponential, $e^{t/\tau}$.
336 That growth rate decreases towards zero as the oxyl fully forms and a limiting coverage is reached. As
337 cartooned in Figure 1, the process is initially barrier less, but as the reaction coordinate extends to form
338 the oxyl, an activation barrier grows in. Since the formation of the oxyl in the theoretical calculation
339 requires a $\sim 10\%$ extension of the titanium-oxygen bond^{12, 22}, an activation barrier would be anticipated
340 for the fully formed oxyl due to the polarization that traps the hole. In terms of the ergodicity of the hole-
341 trapping reaction, there is no barrier to release energy to the surroundings initially and that grows as the
342 equilibrium reaction coordinate of the oxyl forms.

343 Another way to understand how the growth rate slows is through the interaction between oxyls. In the
344 experiments, a population of oxyls is created and this population saturates with photoexcitation fluence,
345 as shown previously. Since a larger population of photoexcited holes does not create a larger oxyl popu-
346 lation, the oxyl coverage is surface limited^{11, 15}. Likely, this surface limitation comes from their repulsive
347 Coulombic interaction. To what extent repulsive interactions between a surface coverage of oxyls or the
348 reaction coordinate polarization itself leads to the observed logistic growth would require atomistic sim-
349 ulations of the hole-trapping event.

350 Finally, we shortly comment on these results from the perspective of Marcus theory of electron transfer
351 for molecules on the one hand, and polaronic distortions in solids on the other. Marcus theory describes
352 how molecular distortions within the molecule and its surroundings lead to a reorganization energy and
353 driving force for electron transfer that together define its transition state and activation barrier³⁰. The
354 reaction kinetics then follow a well-defined law that can be modulated experimentally by, for example,
355 the solvent environment and bonding within the molecule. Ultrafast optical spectroscopy has played an
356 important role in defining the scope of the theory by measuring electron transfer kinetics as a function of
357 these parameters. However, Marcus theory deals with two states—an initial and final one—with a single

358 activation barrier and so, it is not immediately clear how to apply the theory to a dynamically evolving
359 one. On the other hand, more recently, ultrafast x-ray³¹ and multi-dimensional, optical spectroscopy³² of
360 molecular electron transfer depict a multitude of dynamic structural distortions involved in forming the
361 final reaction coordinate. On the solid-state side, ultrafast x-ray diffraction probes polaronic distortions
362 and especially in the halide perovskites³³⁻³⁴. The closest study we are aware of to a dynamic activation
363 barrier are those that measure a radially expanding strain field due to picosecond polaron formation and
364 its subsequent relaxation; corresponding ultrafast optical spectroscopy further associates a time-dependent
365 effective mass³³.

366 CONCLUSIONS

367 The work identifies the formation of an excited state PES that reaches a meta-stable equilibrium for an
368 oxyl radical surface coverage. As such, it describes how stable reactive oxygen intermediates form for
369 oxygen evolution catalysis, among other important catalytic reactions. The formation of the excited state
370 PES is identified through the increasing cross-section of a vibration coupled to its immediate surround-
371 ings. The coupling allows a Fano resonance and its associated parameters to be applied to the time-
372 evolution of the spectral kinetics. Through the fitting of these parameters by the logistic function, the
373 time dynamics show that holes initially trap with barrier-less kinetics until an activation barrier accumu-
374 lates as the polarization due to a distorted reaction coordinate grows; the rates likely depend also on the
375 Coulombic interaction between the trapped holes or oxyls.

376 EXPERIMENTAL METHODS:

377 **Sample and ATR Cell:** 0.7% Nb-doped by weight SrTiO₃ single crystal samples with a (100) crystallo-
378 graphic orientation were acquired from MTI. The crystals measured 10 mm x 10 mm x 0.5 mm in size,
379 with the front side of the sample polished to an arithmetic mean roughness of 0.5 Å.

380
381 For each measurement a custom-built ATR cell made of PEEK plastic was employed, shown in Figure
382 S1. The internal reflection element (IRE) used was a single-bounce 45° trapezoidal diamond (GladiATR
383 plate, Piketech) with a 1 mm front facet and 1.4 mm side facets. The STO samples were mounted within
384 the cell using epoxy (Loctite 615). While the epoxy was still wet, the sample was lightly pressed against
385 the IRE using a Thorlabs Polaris P20 actuator and allowed to fully dry, ensuring the crystals' alignment
386 was parallel with the IRE.

387
388 **Transient Infrared Setup:** The pump and probe beams were generated using a Legend Coherent Elite
389 amplifier Ti:sapphire laser, emitting 800 nm pulses with a temporal width of 150 fs and a repetition rate
390 of 1 kHz. A portion of the light was directed through a 0.5 kHz chopper and then converted through third
391 harmonic generation to a 266 nm pump beam. The pump was directed through the front facet of the IRE
392 at normal incidence to excite the STO sample. Before reaching the IRE, the pump was focused and atten-
393 uated using a focusing lens and variable OD filters, resulting in a beam size of 665 μm FWHM with a
394 fluence of 0.1 mJ/cm² at the sample position. With a 400 fs pulse beam width determined by a cross-
395 correlation (IRF in Figure S3a), this results in a peak fluence in the diamond of 1.14 GW/cm².

396
397 Another portion of the 800 nm pulse was directed into an optical parametric amplifier (Opera Solo) to
398 convert the light to infrared pulses with a center wavelength of 800 cm⁻¹ and a 150 cm⁻¹ bandwidth with
399 P polarization. This polarization has a component perpendicular to sample and allows for exciting the
400 oxyl vibrational mode that is likewise perpendicular to the sample surface. The IR beam was then split
401 using a 50/50 beam splitter to create a probe and reference line. The probe, with a beam size of 350 μm
402 FWHM, was sent through the IRE in the ATR cell at an incidence angle of 60° using a focusing lens. This

403 resulted in an evanescent wave penetration depth of 1.1 μm at the diamond/air interface used for meas-
404 urements.

405
406 After passing through the IRE, the probe was collimated and focused into an entrance slit for an Acton
407 SP-2300 spectrograph (Princeton Instruments), where it was dispersed onto the top row of a dual-array
408 64-element detector (MCT-12-64, Infrared Associates). The reference beam was directed to the bottom
409 array of the detector. The signal was amplified using a boxcar amplifier (FPAS boxcar integrator) and
410 sent to a computer. The delay between pump and probe pulses was controlled by a delay stage (MTM
411 250CC1, Newport). The probe was normalized using the reference line to account for shot-by-shot dif-
412 ferences.

413 **Transient IR ATR measurements:** During the experiments, the sample was pressed into the 1.1 μm
414 penetration depth of the evanescent wave at the diamond/air interface using the actuator. The sample was
415 photoactivated by the 266 nm 0.5 kHz pump and probed with the IR 800 cm^{-1} 1 kHz probe. The absorb-
416 ance was calculated using Beer's Law with $\Delta A = -\log(\Delta R/R)$, where ΔR is the change in reflectivity before
417 and after exciting with the pump, and R is the initial reflection before excitation, measuring the change in
418 reflectance of the sample before and after being pumped. Spectra were collected with a 67 fs step across
419 the desired time range. Following each experiment, the sample was removed from the evanescent wave
420 and a transient background was recorded under the same experimental conditions.

421 ASSOCIATED CONTENT

422 Supporting Information

423 See the supporting information for further detail on experimental design diagrams (Figure S1), analysis procedures (Figures S2-S3, S7), comparisons
424 of repeat trials (Figures S4, S6, S8), Fano fits (Figure S5), all individual and average logistic fit parameters (Table S1, Figure S9), and the comparison
425 of logistic and exponential fits (Figure S10).

426 AUTHOR INFORMATION

427 Corresponding Author

428 * Department of Chemistry and Renewable and Sustainable Energy Institute (RASEI), University of Colorado, Boulder, Boulder, Colorado 80303,
429 United States; Materials Science and Engineering Program, University of Colorado, Boulder, Boulder, Colorado 80303, United States; or-
430 cid.org/0000-0002-1635-2946; Email: tanja.cuk@colorado.edu

431 Author Contributions

432 ^xThese authors contributed equally.

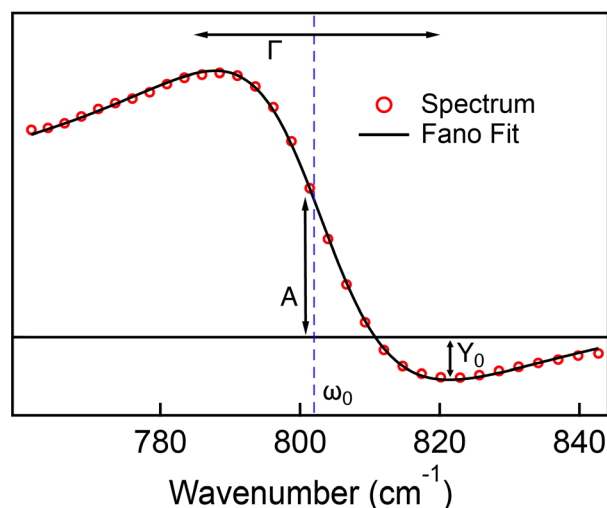
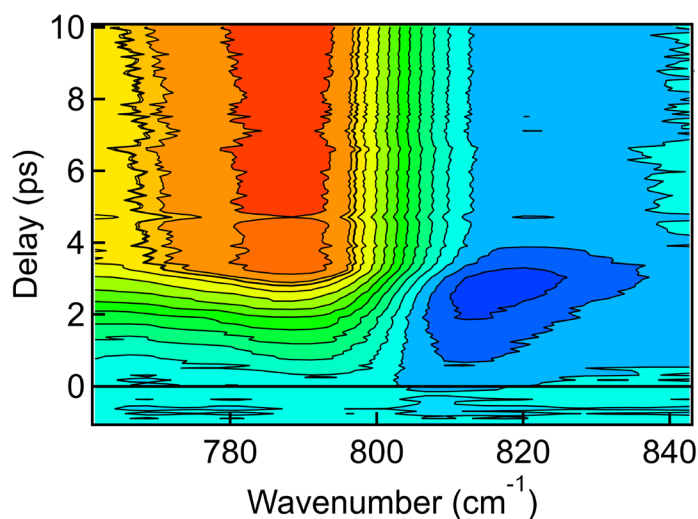
433 DATA AVAILABILITY

434 The data that support the findings of this study are available from the corresponding author upon reasonable request.

435 ACKNOWLEDGMENT

436 The experimental work involved in updating the experimental setup, taking the data, and the analysis was supported by the Director, Office
437 of Science, Office of Basic Energy Sciences, and by the Division of Chemical Sciences, Geosciences and Biosciences of the U.S. Department
438 of Energy at RASEI (Boulder, CO) under Contract No. DE-SC0018939. Modelling of the Fano parameters and the non-equilibrium transient
439 was supported by the Director, Office of Science, Office of Basic Energy Sciences, and by the Division of Materials Sciences and Engineering
440 Division at RASEI (Boulder, CO), under Contract DE-AC02-76SF00515. We thank Thomas Devereaux for helpful discussions on the matter.

441 Authors are required to submit a graphic entry for the Table of Contents (TOC) that, in conjunction with the manuscript title, should
442 give the reader a representative idea of one of the following: A key structure, reaction, equation, concept, or theorem, etc., that is dis-
443 cussed in the manuscript. Consult the journal's Instructions for Authors for TOC graphic specifications.



444

445

446

447

448

449

450

451

452

453

454

455

456

457

458

459

460

461

462

463

464

465

466

467

468

469

470

471

472

473

474

475

476

477

1. Kern, J.; Chatterjee, R.; Young, I. D.; Fuller, F. D.; Lassalle, L.; Ibrahim, M.; Gul, S.; Fransson, T.; Brewster, A. S.; Alonso-Mori, R.; Hussein, R.; Zhang, M.; Douthit, L.; de Lichtenberg, C.; Cheah, M. H.; Shevela, D.; Wersig, J.; Seuffert, I.; Sokaras, D.; Pastor, E.; Wening, C.; Kroll, T.; Sierra, R. G.; Aller, P.; Butryn, A.; Orville, A. M.; Liang, M.; Batyuk, A.; Koglin, J. E.; Carbajo, S.; Boutet, S.; Moriarty, N. W.; Holton, J. M.; Dobbek, H.; Adams, P. D.; Bergmann, U.; Sauter, N. K.; Zouni, A.; Messinger, J.; Yano, J.; Yachandra, V. K., Structures of the intermediates of Kok's photosynthetic water oxidation clock. *Nature* **2018**, *563* (7731), 421-425.
2. Banin, U.; Waiskopf, N.; Hammarstrom, L.; Boschloo, G.; Freitag, M.; Johansson, E. M. J.; Sa, J.; Tian, H.; Johnston, M. B.; Herz, L. M.; Milot, R. L.; Kanatzidis, M. G.; Ke, W.; Spanopoulos, I.; Kohlstedt, K. L.; Schatz, G. C.; Lewis, N.; Meyer, T.; Nozik, A. J.; Beard, M. C.; Armstrong, F.; Megarity, C. F.; Schmuttenmaer, C. A.; Batista, V. S.; Brudvig, G. W., Nanotechnology for catalysis and solar energy conversion. *Nanotechnology* **2021**, *32* (4).
3. Liu, H.; Frei, H., Observation of O–O Bond Forming Step of Molecular Co₄O₄ Cubane Catalyst for Water Oxidation by Rapid-Scan FT-IR Spectroscopy. *ACS Catalysis* **2020**, *10* (3), 2138-2147.
4. Zhang, M.; Frei, H., Towards a Molecular Level Understanding of the Multi-Electron Catalysis of Water Oxidation on Metal Oxide Surfaces. *Catalysis Letters* **2014**, *145* (1), 420-435.
5. Aschaffenburg, D. J.; Kawasaki, S.; Pemmaraju, C. D.; Cuk, T., Accuracy in Resolving the First Hydration Layer on a Transition-Metal Oxide Surface: Experiment (AP-XPS) and Theory. *The Journal of Physical Chemistry C* **2020**, *124* (39), 21407-21417.
6. Ketteler, G.; Yamamoto, S.; Bluhm, H.; Andersson, K.; Starr, D. E.; Ogletree, D. F.; Ogasawara, H.; Nilsson, A.; Salmeron, M., The nature of water nucleation sites on TiO₂(110) surfaces revealed by ambient pressure X-ray photoelectron spectroscopy. *J. Phys. Chem. C* **2007**, *111* (23), 8278-8282.
7. Hammes-Schiffer, S., Proton-Coupled Electron Transfer: Moving Together and Charging Forward. *Journal of the American Chemical Society* **2015**, *137* (28), 8860-8871.
8. Cukier, R. I.; Nocera, D. G., PROTON-COUPLED ELECTRON TRANSFER. *Annual Review of Physical Chemistry* **1998**, *49* (1), 337-369.

- 478 9. Pham, H. H.; Cheng, M.-J.; Frei, H.; Wang, L.-W., Surface Proton Hopping and Fast-Kinetics
479 Pathway of Water Oxidation on Co₃O₄(001) Surface. *ACS Catalysis* **2016**, *6* (8), 5610-5617.
- 480 10. Chen, X.; Aschaffenburg, D. J.; Cuk, T., Selecting between two transition states by which water
481 oxidation intermediates decay on an oxide surface. *Nature Catalysis* **2019**, *2* (9), 820-827.
- 482 11. Chen, X.; Choing, S. N.; Aschaffenburg, D. J.; Pemmaraju, C. D.; Prendergast, D.; Cuk, T., The
483 formation time of Ti-O• and Ti-O•-Ti radicals at the n-SrTiO₃/aqueous interface during photocatalytic
484 water oxidation. *Journal of the American Chemical Society* **2017**, *139*, 1830-1841.
- 485 12. Herlihy, D. M.; Waegele, M. M.; Chen, X.; Pemmaraju, C. D.; Prendergast, D.; Cuk, T., Detecting
486 the oxyl radical of photocatalytic water oxidation at an n-SrTiO₃/aqueous interface through its subsurface
487 vibration. *Nat Chem* **2016**, *8* (6), 549-55.
- 488 13. I. Vinogradov; S. Singh; H. Lyle; A. Mandal*; J. Rossmeisl; Cuk*, T., Measuring theoretical
489 descriptors of water oxidation: Free energy differences between intermediates by time-resolved optical
490 spectroscopy. *Nature Materials, Under-revision* **2020**, (Preprint at ChemRxiv).
- 491 14. Waegele, M. M.; Chen, X.; Herlihy, D. M.; Cuk, T., How Surface Potential Determines the
492 Kinetics of the First Hole Transfer of Photocatalytic Water Oxidation. *Journal of the American Chemical*
493 *Society* **2014**, *136* (30), 10632-10639.
- 494 15. S. Singh, H. L., L. D'Amario, E. Magnano, I. Vinogradov, & T. Cuk, Coherent acoustic
495 interferometry during the photo-driven oxygen evolution reaction associates strain fields with the reactive
496 oxygen intermediate (Ti-OH*). *J. Am. Chem. Soc.* **2021**, Submitted (ChemRXiv. Preprint.
497 <https://doi.org/10.26434/chemrxiv.14550912.v1>).
- 498 16. Fano, U., Effects of Configuration Interaction on Intensities and Phase Shifts. *Physical Review*
499 **1961**, *124* (6), 1866-1878.
- 500 17. Frontiera, R. R.; Gruenke, N. L.; Van Duyne, R. P., Fano-Like Resonances Arising from Long-
501 Lived Molecule-Plasmon Interactions in Colloidal Nanoantennas. *Nano Letters* **2012**, *12* (11), 5989-5994.
- 502 18. Yang, W.; Liu, Y.; Edvinsson, T.; Castner, A.; Wang, S.; He, S.; Ott, S.; Hammarström, L.; Lian,
503 T., Photoinduced Fano Resonances between Quantum Confined Nanocrystals and Adsorbed Molecular
504 Catalysts. *Nano Letters* **2021**, *21* (13), 5813-5818.
- 505 19. Austin, I. G.; Mott, N. F., Polarons in crystalline and non-crystalline materials. *Advances in*
506 *Physics* **2001**, *50* (7), 757-812.
- 507 20. Janotti, A.; Varley, J. B.; Choi, M.; Van de Walle, C. G., Vacancies and small polarons in SrTiO₃.
508 *Phys. Rev. B* **2014**, *90* (8), 085202.
- 509 21. Schirmer, O. F., O-bound small polarons in oxide materials. *Journal of Physics: Condensed*
510 *Matter* **2006**, *18* (43), R667-R704.
- 511 22. Cheng, J.; VandeVondele, J.; Sprik, M., Identifying Trapped Electronic Holes at the Aqueous
512 TiO₂ Interface. *J. Phys. Chem. C* **2014**, *118* (10), 5437-5444.
- 513 23. Chen, X.; Aschaffenburg, D.; Cuk, T., One-electron intermediates of water oxidation & the role
514 of solvation in their stability. *J. Mater. Chem. A* **2017**, *5* (23), 11410-11417.
- 515 24. Milosevic, M., *Internal Reflection and ATR Spectroscopy*. Wiley: 2012.
- 516 25. Fischer, B.; Bäuerle, D.; Buckel, W. J., Surface polaritons in KTaO₃ and SrTiO₃. *Solid State*
517 *Communications* **1974**, *14* (3), 291-294.
- 518 26. Roth, T.; Laenen, R., Absorption of free carriers in diamond determined from the visible to the
519 mid-infrared by femtosecond two-photon absorption spectroscopy. *Optics Communications* **2001**, *189*
520 (4), 289-296.
- 521 27. Dadap, J. I.; Focht, G. B.; Reitze, D. H.; Downer, M. C., Two-photon absorption in diamond and
522 its application to ultraviolet femtosecond pulse-width measurement. *Optics letters* **1991**, *16* (7), 499-501.
- 523 28. Gervais, F.; Servoin, J. L.; Baratoff, A.; Bednorz, J. G.; Binnig, G., Temperature dependence of
524 plasmons in Nb-doped SrTiO₃. *Physical review. B, Condensed matter* **1993**, *47* (13), 8187-8194.
- 525 29. Reed, L. J.; Berkson, J., The Application of the Logistic Function to Experimental Data. *The*
526 *Journal of Physical Chemistry* **1929**, *33* (5), 760-779.
- 527 30. Marcus, R. A.; Sutin, N., Electron transfers in chemistry and biology. *Biochimica et Biophysica*
528 *Acta (BBA) - Reviews on Bioenergetics* **1985**, *811* (3), 265-322.

- 529 31. Cammarata, M.; Bertoni, R.; Lorenc, M.; Cailleau, H.; Di Matteo, S.; Mauriac, C.; Matar, S. F.;
530 Lemke, H.; Chollet, M.; Ravy, S.; Laulhé, C.; Létard, J.-F.; Collet, E., Sequential Activation of Molecular
531 Breathing and Bending during Spin-Crossover Photoswitching Revealed by Femtosecond Optical and X-
532 Ray Absorption Spectroscopy. *Physical Review Letters* **2014**, *113* (22), 227402.
- 533 32. Gaynor, J. D.; Sandwisch, J.; Khalil, M., Vibronic coherence evolution in multidimensional
534 ultrafast photochemical processes. *Nature Communications* **2019**, *10* (1), 5621.
- 535 33. Guzelturk, B.; Winkler, T.; Van de Goor, T. W. J.; Smith, M. D.; Bouelle, S. A.; Feldmann, S.;
536 Trigo, M.; Teitelbaum, S. W.; Steinrück, H.-G.; de la Pena, G. A.; Alonso-Mori, R.; Zhu, D.; Sato, T.;
537 Karunadasa, H. I.; Toney, M. F.; Deschler, F.; Lindenberg, A. M., Visualization of dynamic polaronic
538 strain fields in hybrid lead halide perovskites. *Nature Materials* **2021**, *20* (5), 618-623.
- 539 34. Seiler, H.; Zahn, D.; Taylor, V. C. A.; Bodnarchuk, M. I.; Windsor, Y. W.; Kovalenko, M. V.;
540 Ernstorfer, R., Direct Observation of Ultrafast Lattice Distortions during Exciton–Polaron Formation in
541 Lead Halide Perovskite Nanocrystals. *ACS Nano* **2023**, *17* (3), 1979-1988.

542
